Silicon subwavelength grating waveguides with high-index chalcogenide glass cladding

Philippe Jean, Alexandre Douaud, Sophie LaRochelle, Younès Messaddeq, and Wei Shi

OSA Optics Express, (Vol. 29, No. 13) (21 June 2021)

https://doi.org/10.1364/OE.430204

Research Article | Vol. 29, No. 13 / 21 June 2021 / Optics Express 20851

Optics EXPRESS

Silicon subwavelength grating waveguides with high-index chalcogenide glass cladding

PHILIPPE JEAN,[1,2] ALEXANDRE DOUAUD,[1] SOPHIE LAROCHELLE,[1,2] YOUNÈS MESSADDEQ,[1,3] AND WEI SHI[1,2,*]

[1]Centre d'Optique, Photonique et Laser (COPL), 2375 rue de la Terrasse, Université Laval, Québec G1V 0A6, Canada
[2]Département de Génie Électrique et de Génie Informatique, Université Laval, 2325, rue de l'Université, Québec G1V 0A6, Canada
[3]Département de Physique, de Génie Physique et d'Optique, Université Laval, 2325, rue de l'Université, Québec G1V 0A6, Canada
[*]wei.shi@gel.ulaval.ca

Abstract: Silicon subwavelength grating waveguides enable flexible design in integrated photonics through nano-scale refractive index engineering. Here, we explore the possibility of combining silicon subwavelength gratings waveguides with a high-index chalcogenide glass as a top cladding, thus modifying the waveguiding behavior and opening a new design axis for these structures. A detailed investigation of the heterogeneous SWG waveguide with high-index cladding is presented based on analytical and numerical simulations. We design, fabricate and characterize silicon subwavelength grating waveguide microring resonators with an $As_{20}S_{80}$ cladding. Thanks to $As_{20}S_{80}$ negative thermo-optic coefficient, we achieve near athermal behavior with a measured minimum thermally induced resonance shift of −1.54 pm/K, highlighting the potential of subwavelength grating waveguides for modal confinement engineering and to control light-matter interaction. We also show that the chalcogenide glass can be thermally reflowed to remove air gaps inside the cladding, resulting in a highly conformal structure. These types of waveguides can find application in reconfigurable photonics, nonlinear optics, metamaterials or slow light.

1. Introduction

Advances in fabrication technology have put forward the potential of controlling light at the subwavelength scale in order to boost the performance and flexibility of integrated optic components. To this end, silicon subwavelength grating waveguides (SWGs) are a prominent example of subwavelength engineering that led to substantial performance improvements in practical applications [1]. SWGs are one-dimensional periodic waveguides with feature size that are much smaller than their operating wavelengths, such that the relation $\lambda >> 2n_{eff}\Lambda$ approximately holds [2]. As such, they support the diffraction-less propagation of a Bloch mode, whose properties can be controlled through not only careful design of their cross-sections but also by controlling the period Λ and the duty-cycle $DC = L_{Si}/\Lambda$.

The added degrees of freedom of SWG provide more flexibility in their design; in the deep subwavelength limit, light sees the grating as an homogeneous material with a weighted refractive index, thus opening the possibility of refractive index engineering [3]. Index engineering can be used to multiple ends. A few key examples include on-chip control of group delay [4,5], bandwidth increase of contra-directional couplers [6] or of multimode interferometers [7], on-chip polarization management [7–9], polarization-independent and efficient fiber-to-chip edge couplers [10,11] and engineering of the bandwidth of Bragg filters [12].

In addition to index engineering, SWGs are also interesting to control light-matter interaction with the waveguide top cladding, which can be air or an analyte for sensing [13,14], a material

#430204 https://doi.org/10.1364/OE.430204
Journal © 2021 Received 28 Apr 2021; revised 2 Jun 2021; accepted 9 Jun 2021; published 17 Jun 2021

Optics EXPRESS

with a negative thermo-optic coefficient *TOC* for thermal compensation [15] or even a potential rare-earth ions host for amplification [16]. The use of exotic cladding materials is therefore a promising emergent topic with potential to add another degree of freedom in designing SWGs. Among the materials that are amenable for heterogeneous integration with SWG, chalcogenide glasses (ChG) present a set of unique and attractive properties for photonics, including low-loss over a large transparency window, photosensitivity, high non-linearity and a high refractive index [17]. Chalcogenides are also excellent materials for the important field of Brillouin photonics as their low density allow for acoustic waveguiding in addition to optical waveguiding [18]. The development of hybrid chalcogenide-silicon waveguides is a promising approach to harness interesting chalcogenide properties on the silicon platform [19,20].

In this work, we study the combination of silicon SWGs with a high-index chalcogenide glass top cladding. The effect of using a high-index material is first explored through analytical methods. A novel $As_{20}S_{80}$-on-Si SWG design is demonstrated using the finite-difference time domain (FDTD) method. Next, microring resonators (MR) based on the designed waveguide are fabricated. The passive optical properties and thermal response of the fabricated MR are measured at telecommunication wavelengths. The MR exhibit intrinsic quality factor of $Q = 5.6 \times 10^4$ and athermal behavior with a slightly negative wavelength shift of $\Delta\lambda_r/\Delta T = -1.54$ pm/K. We also demonstrate that the use of a chalcogenide soft glass can eliminate the formation of air gaps inside the cladding.

2. SWG with high-index claddings

2.1. 1D analytical model

In contrast with conventional 2D waveguides (e.g. strips or ribs), SWGs support the propagation of a Bloch mode with properties that are affected by the periodic nature of the waveguide permittivity. Therefore, 2D simulation methods like finite difference eigenmode (FDE) cannot fully capture the intricacy of SWGs optical properties. Rigorous 3D simulation methods like finite-difference time domain (FDTD) can be used to accurately predict the waveguides behavior, but they are computationally expensive and time consuming. Insight into the Bloch mode behavior and initial design guidelines can be obtained by realizing that the peculiarities of the SWGs are akin to the propagation of a plane wave inside a periodic dielectric stack that is semi-infinite in the transversal directions, hereafter referred to as a Bragg stack (BS). The basic features of Bloch mode propagation can then be modelled using an analytical 1D approach. A BS with alternating material permittivities $\epsilon_1 = n_1^2$ and $\epsilon_2 = n_2^2$ and period Λ is schematically shown in the inset (i) of Fig. 1(a). At normal incidence, the dispersion relation of a BS is given as [21,22]

$$\cos(K\Lambda) = \cos(k_1 l_1)\cos(k_2 l_2) - \frac{(n_1^2 + n_2^2)}{(2n_1 n_2)}\sin(k_1 l_1)\sin(k_2 l_2), \tag{1}$$

where K is the Bloch mode propagation constant and $k_{1,2} = \frac{2\pi n_{1,2}}{\lambda}$ is the wavenumber. The length of each material is given as $l_1 + l_2 = \Lambda$ and the duty-cycle, or filling factor, is $DC = l_1/\Lambda$. For the specific case of this work, ϵ is considered real as the materials absorption are neglected, but we note that they can be included by simply considering an imaginary part to ϵ [22]. The relation of Eq. (1) is limited in two ways: (1) it ignores the effect of transversal confinement, which is substantial in high-index contrast waveguides and (2) it considers a crystal that extends to infinity along the propagation axis. The first limitation can be easily solved by using 3D methods, as previously mentioned. The finite nature of real devices, on the other hand, requires careful design of the tapers to efficiently inject into Bloch modes from standard waveguide modes [23,24]. Nevertheless, such a simplified model can provide insight into the behavior of SWG at negligible computational cost and serve as an initial design tool.

Optics EXPRESS

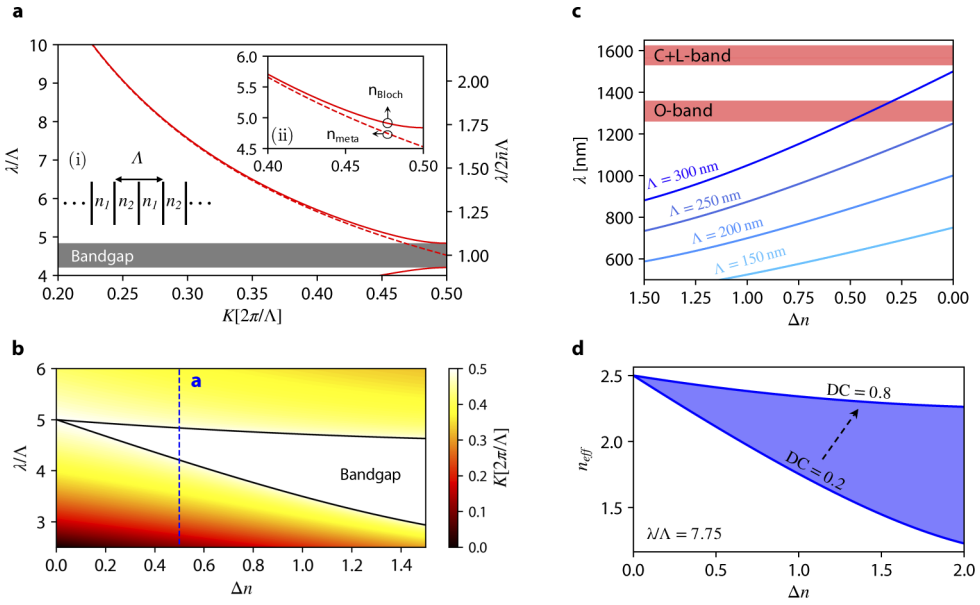

Fig. 1. Propagation of the Bloch mode in a dielectric stack. (a) Bandstructure simulated using the analytical model of Eq. (1) (solid line) and using a metamaterial approximation (dashed line) with a fixed index contrast $\Delta n = 0.5$. Inset (i): 1D geometry of the BS. Inset (ii): Close-up view near the bandgap showing the deviation between the model of Eq. (1) and the metamaterial approximation (see text). (b) Map of the Bloch mode normalized propagation constant for varying refractive index contrast between the stacks. The vertical dashed line indicates the geometry for which the bandstructure is shown in (a) and the black solid lines delimit the extent of the bandgap. (c) Band-edge location in an infinite crystal with different minimum periods. The minimum feature size for $DC = 0.5$ is half the period $\Lambda/2$. The red shaded regions highlight commonly used spectral bands in telecommunications. (d) Engineering the effective index by tuning the material index and the waveguide duty-cycle DC. The normalized wavelength is fixed at $\lambda/\Lambda = 7.75$.

The effect of high-index cladding is first explored using Eq. (1) by setting n_2 as the cladding material refractive index with a constant $n_1 = 2.5$ to represent the index of the silicon period, close to the effective index of a 500 nm wide silicon nanowire at 1550 nm. The effect of index contrast $\Delta n = |n_1 - n_2|$ on the propagation properties is summarized in Fig. 1(a) through (d). The bandstructure near the first order bandgap of a BS with $\Delta n = 0.5$ and $DC = 0.5$ is shown in Fig. 1(a). The result obtained from Eq. (1) is compared with a metamaterial approximation $n^2_{meta} = \Lambda^{-1}(l_1\epsilon_1 + l_2\epsilon_2)$. As expected, the BS propagation constant K tends toward that using the metamaterial in the deep-subwavelength $\lambda >> \Lambda$ but deviates significantly when approaching the bandgap.

The main effect of reducing the index contrast is the narrowing of the bandgap, as seen in Fig. 1(b), which is expected as the BS approaches a uniform medium in the limit $\Delta n \to 0$. This narrowing is accompanied by a shift of the band-edges λ_{BE}, the blue- and red-side wavelength boundaries of the bandgap, which effectively limits the operation in the deep-subwavelength regime at a given wavelength. This is important considering that the minimum feature size of electron-beam lithography and UV photolithography are about 60 nm and 150 nm, respectively. The fabrication minimum feature size then puts a hard limit on how far away from the bandgap the waveguide can be designed to operate. It is well known that silicon SWG do not really operate in the deep-subwavelength regime, where they could be treated using an effective medium

Optics EXPRESS

theory, but are effectively operating in the transition region [1]. In Fig. 1(c), the position of the red-side band-edge λ_{BE} is plotted for various Λ and refractive index contrast Δn. With $DC = 0.5$, the minimum feature size required is half the period $\Lambda/2$. It is clear that one must be careful when using high-index materials with SWGs as the band-edge creeps rapidly towards common operating wavelengths in the O-band or C-band, for example. We also note that proximity to the band-edge is to be carefully considered, as even if the light is not diffracted in the bandgap, multiple scattering, slow light and Bloch mode reshaping can drastically increase the propagation losses [5,25]. The extent to which the effective index of a BS operating in the SWG regime ($\lambda/\Lambda = 7.75$) can be engineering is shown in Fig. 1(d). A large span of effective index can be achieved by tuning the SWG duty-cycle and using cladding materials with different refractive index.

The analytical model of Eq. (1) is then used to study the effect of high-index cladding on the optical field distribution inside the BS. We use the dimensionless confinement factor Γ_i, describing the interaction between the Bloch mode and material i such as [26,27]

$$\Gamma_i = \frac{n_g}{n_i} \frac{\int_i \epsilon |\mathbf{E}|^2 \, dV}{\int \epsilon |\mathbf{E}|^2 \, dV}, \tag{2}$$

where n_g is the group index, n_i is the material for which Γ_i is considered, ϵ is the dielectric permittivity and $\mathbf{E}$ is the vectorial electric field. The integral in Eq. (2) is taken over the volume V of a single unit-cell. For the BS, the integral reduce to a single dimension. We note that Γ_i really consider two distinct effects, the slow light enhancement and the energy density distribution. While the second takes value between 0 and 1, the slow light enhancement results in $\Gamma>1$ near the bandgap [26].

The normalized wavelength dependence of Γ is presented using an analogue to the bandstructure in Fig. 2(a), with the different operation regions identified for clarity. In the deep-subwavelength limit, the confinement factor is directly proportional to the material index and to the duty-cycle, indicating a uniform distribution of the field over the unit cell or, in other words, that the periodicity does not affect the mode distribution. The effect of periodicity becomes significant in the transition region, where Γ_{Si} increases until it diverges at the band-edge. This is associated with a reshaping of the Bloch mode and increased(decreased) interaction with the high(low)-index material. This behavior of enhanced light-matter interaction near the band-edge of photonic crystals is responsible for a variety of interesting effects, including gain enhancement for lasers [28] or the optical Borrmman effect [29]. Fig. 2(b) shows the normalized electric field intensity inside along the propagation axis of one unit cell for various parameters, highlighting the mode redistribution into the high index period due to both the wavelength dependence (left panel) and the index contrast (right panel). The sharp increase of Γ_{Si} and associated decrease of Γ_{clad} in the transition region have consequences in applications where the SWG is used to enhance interaction with the cladding material, such as in thermal compensation [15]. The effect of thermally induced perturbations are important for integrated optics in general and relevant in the context of ChG functionalization [30–32]. Using the confinement factors, the effective thermo-optic coefficient $TOC_{eff} = dn_{eff}/dT$ can be calculated to a first-order approximation as [32]

$$\frac{dn_{eff}}{dT} \approx \Gamma_1 \frac{dn_1}{dT} + \Gamma_2 \frac{dn_2}{dT}. \tag{3}$$

In this work, we consider the case where n_1 is silicon and has a thermo-optic coefficient of $dn_{Si/1}/dT = 1.8 \times 10^{-4}$ RIU/K [33] while the material n_2 is $As_{20}S_{80}$, with $n_2 = n_{As_{20}S_{80}} = 2.15$ and $dn_{ChG/2}/dT = -5 \times 10^{-5}$ [31].

Optics EXPRESS

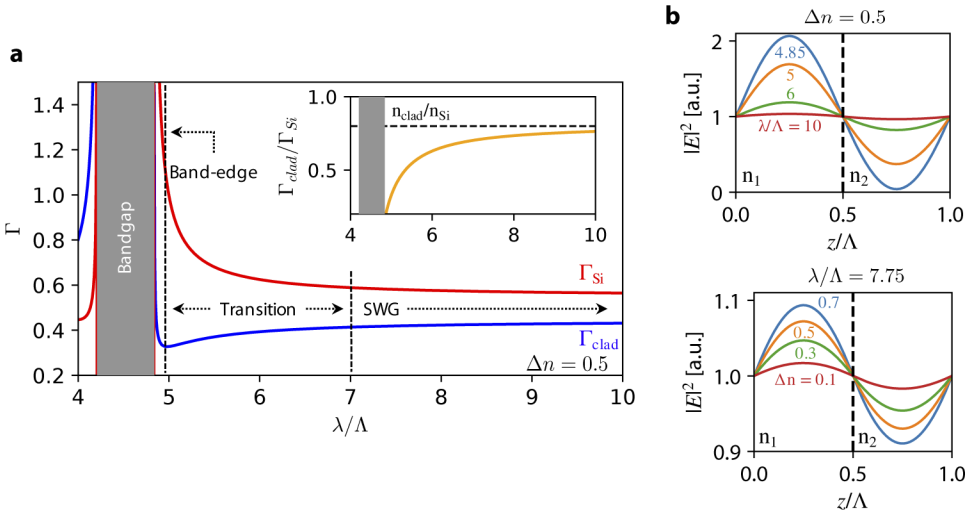

Fig. 2. Confinement factor of the Bloch mode in a dielectric stack simulated using the model of Eq. (1). (a) Confinement factor in the silicon (red solid line) and in the glass (solid blue line) as a function of normalized wavelength λ/Λ with a fixed $\Delta n = 0.5$. The vertical dashed lines serve to approximately delimit the operation regions (SWG, transition and band-edge). The bandgap is indicated as the dark grey area. Inset: Confinement factor ratio $\Gamma_{clad}/\Gamma_{Si}$ that tends towards n_2/n_1 in the SWG limit (dashed line). (b) Normalized electric field intensity along one period (top) for various normalized wavelengths $\lambda/\Lambda = [4.85, 5, 6, 10]$ and fixed $\Delta n = 0.5$ and (bottom) for various index contrast $\Delta n = [0.7, 0.5, 0.3, 0.1]$ and fixed $\lambda/\Lambda = 7.75$.

2.2. FDTD simulations

Following the basic design guidelines provided by the analytical simulations of the previous section, we simulated an SWG with a 800 nm $As_{20}S_{80}$ cladding, which is expected to provide thermal compensation while allowing to operate sufficiently far away from the band-edge to avoid detrimental effects. The periodicity in the FDTD simulation was achieved using Bloch boundary conditions along the propagation axis and the simulation time window was 2000 fs (time step of 0.02 fs). The simulation window is 16 μm wide and 8 μm high and the meshing is set to 10 nm in all direcitons around the silicon block. The simulated waveguide parameters are $w = 450$ nm, $t = 220$ nm and $DC = 0.5$. Three periods are considered: $\Lambda = [200, 250, 300]$ nm.

The effective index and group index of the heterogeneous SWG are shown in Fig. 3(a) and (b), respectively. We observe the absence of bandgap related distortion down to at least $\lambda = 1400$ nm for $\Lambda = 200$ nm, so that the SWG is expected to operate in the transition region. The SWG with $\Lambda = 250$ nm shows a moderate increase of n_g at shorter wavelength, indicating operation in the transition region that approaches the bandgap while the SWG with $\Lambda = 300$ nm has its bandgap just short of $\lambda = 1500$ nm. The position of the bandgap is represented as a divergence of the effective and group indices in the plots. The 3D distribution of the electric field intensity at $\lambda = 1550$ nm for $\Lambda = 250$ nm is shown in Fig. 3(c). The relatively narrow waveguide geometry and reduced effective refractive index results in a delocalization of the mode outside of the silicon block in the transversal directions. The right panel of Fig. 3(c) shows a top view where the concentration of $|E|^2$ inside the silicon is clearly visible, indicating that the SWG does not operate in the deep-subwavelength region. The confinement factors are $\Gamma_{Si} = 0.28$, $\Gamma_{clad} = 0.89$ and $\Gamma_{SiO_2} = 0.06$. The thermo-optic coefficient of the waveguide is predicted to be $\frac{dn_{eff}}{dT} = 6.3 \times 10^{-6}$ using the material thermo-optic coefficient (*TOC*) reported in Ref. [31]. This corresponds to

Optics EXPRESS

a resonant wavelength shift of $\Delta\lambda_r/\Delta T$ = 6.2 pm/K in a microring resonator with R = 100 µm. We note that the large ratio of $\Gamma_{clad}/\Gamma_{Si}$>3 in TE polarization is a good example of the SWG advantage in increasing light-matter interaction with top cladding materials.

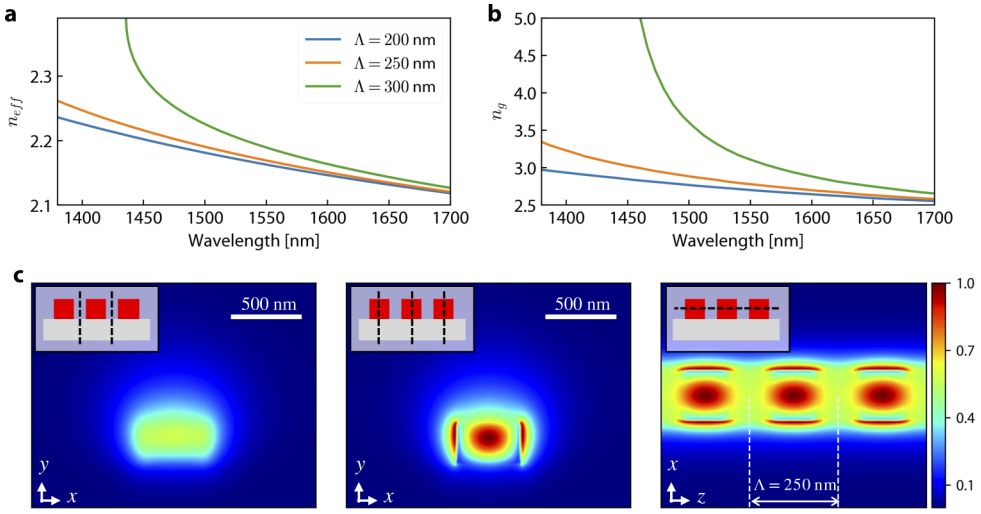

Fig. 3. (a) and (b) Effective index and group index simulated using 3D-FDTD for an $As_{20}S_{80}$ clad SWG with w = 450 nm, DC = 0.5 and different periods(b) Electric field intensity distribution of the Bloch mode for Λ = 250 nm in the (left) xy plane in the glass, (center) xy plane in the Si and (right) zx plane at mid-height in the waveguide for 3 periods.

3. Fabrication

Next, the waveguide simulated using FDTD in the last section was used to design and fabricate microring resonators. MRs were chosen instead of straight waveguides because they provide measurement of the group index, propagation loss and thermo-optic coefficient in a very compact footprint. In addition, estimating the waveguide loss from the MRs response instead of using the cutback methods alleviates the error arising from variations in the fiber-to-chip coupling when depositing the cladding on individual chips. The silicon chips were processed using electron-beam lithography by Applied NanoTools through the SiEPICfab consortium [34] on 220 nm thick silicon-on-insulator wafers with 2 µm thick buried oxide (BOx) layer. The glassy thin-films were deposited in-house using the same method as described in Ref. [31], including the 120 s annealing step at T = 150 °C. The measured deposited cladding thickness is 890 nm. A schematic of the heterogeneous SWG is provided in Fig. 4(a). Scanning electron microscope (SEM) images were taken before the glass deposition. A top view SEM image of an MR is shown in Fig. 4(b) with the inset showing a close-up of the coupling region between the ring and the bus waveguide. The routing strip waveguides (500 nm × 220 nm) were converted into SWGs using linear geometrical tapers of length L_{taper} = 100 µm, similar to those used in [5]. The fabricated device had a radius R = 100 µm, a width w = 450 nm, a period Λ = 250 nm and a duty-cycle DC = 0.5.

A common difficulty when fabricating oxide-clad silicon devices with tiny features like SWGs is the formation of air voids that are not filled by the oxide [35]. These voids can lead to significant performance deviation from the intended design. The use of materials that can be reflowed at low temperature, like chalcogenides, can suppress these gaps and lead to a conformal structure where the cladding material completely covers the silicon. This effect in the $As_{20}S_{80}$ cladded SWGs was investigated using focused ion beam milling (FIB) to image the waveguide

Optics EXPRESS

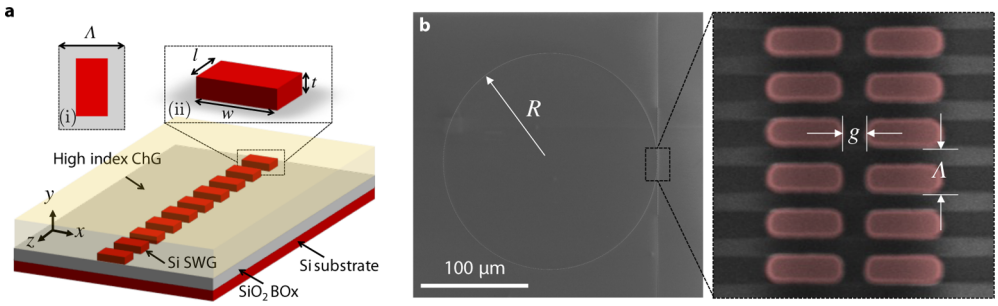

Fig. 4. Silicon SWG waveguides and microresonators with high-index ChG cladding. (a) Schematic drawing of an SWG waveguide with period Λ, width w. Inset (i): Top view of a single unit cell. Inset (ii): Geometry of a single silicon block. (b) Top view SEM image of a fabricated SWG microresonator of radius R with a close-up view of the coupling as inset (right).

along its propagation axis in a sample before annealing (as-deposited) and in a sample after thermal annealing. The as-deposited sample had systematic voids, as visible in Fig. 5(a), where the air appears as darker patterns. Thermal annealing resulted in the reflow of the glass and a complete filling between the silicon blocks, as visible in Fig. 5(b). We note that this aggressive reflow at moderate temperature (T = 150°C) is possible due to the quasi-polymeric behavior of the sulfur-rich chalcogenide composition [36]. A similar effect was reported in silicon slot waveguides covered with As_2S_3 for nonlinear photonics [20].

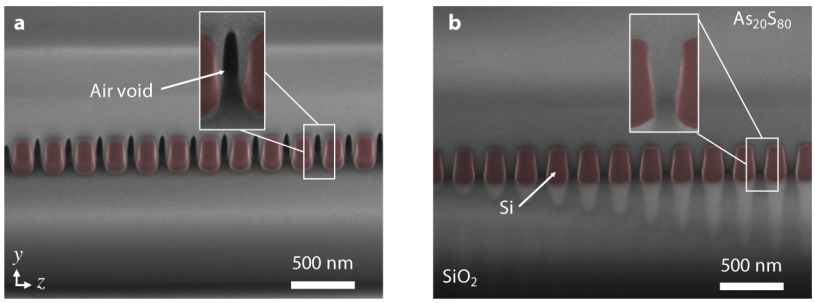

Fig. 5. SEM images of fabricated heterogeneous SWG waveguides with FIB cut along the propagation axis before (a) and after (b) thermal annealing. The insets show close-up views of the glass between the silicon pillars, showing the air gap before annealing and the filling of the gap by the glass after annealing.

4. Optical characterization

4.1. Passive response

The optical response of an SWG MR with g = 300 nm was measured using an optical vector analyzer (OVA5000 from LUNA). The chip stage was mounted on a Peltier module with a temperature controller (TEC) to stabilize the operation at T = 20 °C. The results are summarized in Fig. 6(a) through (d).

The transmittance is shown in Fig. 6(a) while a single resonance is identified and zoomed on in (b). From the resonances, the group index can be calculated and is presented in Fig. 6(d) alongside simulated values using 3D-FDTD. We note that the linear increase of group index with frequency suggests the absence of band-edge proximity effect and operation away from

Optics EXPRESS

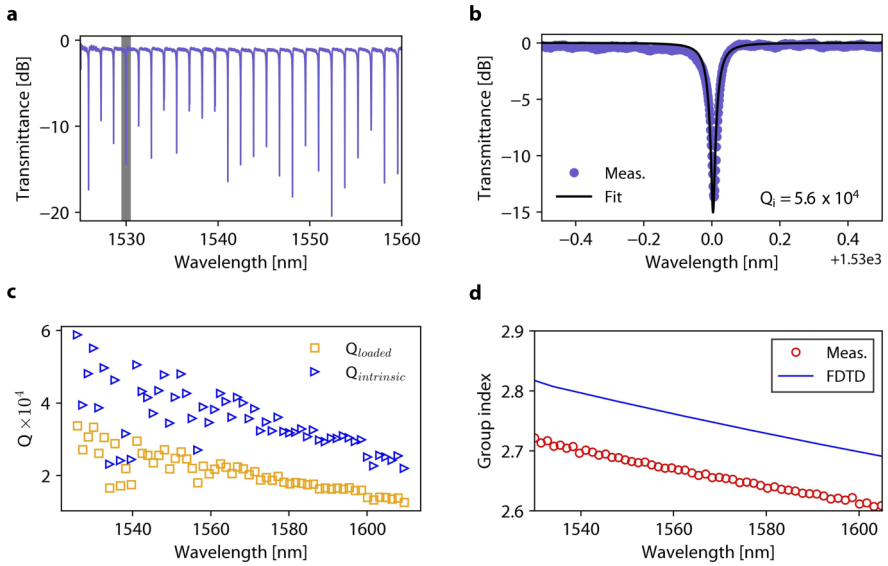

Fig. 6. Passive optical characterization of an $As_{20}S_{80}$ clad SWG microring resonator with $\Lambda = 250$ nm, $DC = 0.5$, $w = 450$ nm and $g = 300$ nm. (a) Normalized transmittance in the C-band. (b) Single resonance with $Q_i = 5.6 \times 10^4$ near 1530 nm (identified as the shaded region in (a)). (c) Quality factors measurement over the C+L band. (d) Measured (red markers) and simulated (blue line) group index over the C+L band.

the bandgap, as expected from the FDTD simulations. The difference between the simulated and measured values of group index could arise from a variety of fabrication errors that are non-trivial to separate. We also mention that the dispersion of $As_{20}S_{80}$ used in the simulations was obtained using a prism-coupling method with a certain degree of uncertainty, which could explain the difference [31]. Next, the waveguiding loss is assessed through the MR quality factor $Q = \lambda/FWHM$, calculated using a Lorentzian fit on each resonance, as in Fig. 6(b). The wavelength dependence of the loaded and intrinsic Q is shown in 6(c). The intrinsic quality-factor Q_i and the associated propagation loss α are calculated using the formulas [37,38]

$$Q_i = \frac{2Q}{1 + \sqrt{T_0}} \approx \frac{2\pi n_g}{\alpha \lambda_{res}}, \tag{4}$$

where T_0 is the normalized transmittance at the resonant wavelength. Eq. (4) assumes undercoupled operation, which is the case for the device considered in this work. Leakage to the substrate is not expected in this geometry due to the mode displacement in the ChG cladding and associated high effective index [16,39]. The reduction of loss at shorter wavelength reinforces the idea that the SWG operates sufficiently far from the band-edge. The highest intrinsic quality-factor measured is $Q_i = 5.6 \times 10^4$ and corresponds to waveguide propagation loss of around $\alpha = 8.6$ dB/cm. The propagation losses are comparable to those recently reported in tellurium dioxide clad SWG [16]. We note that the SWG presented here was specifically designed to operate in TE polarization. The TM polarization in this structure is strongly delocalized and large bending losses are expected even for R = 100 μm. Because of this, the TM response of the MR was not observed in the measurements.

4.2. Thermal response

Finally, the thermal response of the heterogeneous SWG was investigated by increasing the TEC temperature in steps of 3 °C and monitoring the MR resonant wavelength shift. The results are

Optics EXPRESS

summarized in Fig. 7(a) through (d), where (a) and (b) are examples of measurement of two resonances: one at shorter wavelength with a nearly temperature independent behavior and one at longer wavelength with a strong negative dependence, respectively.

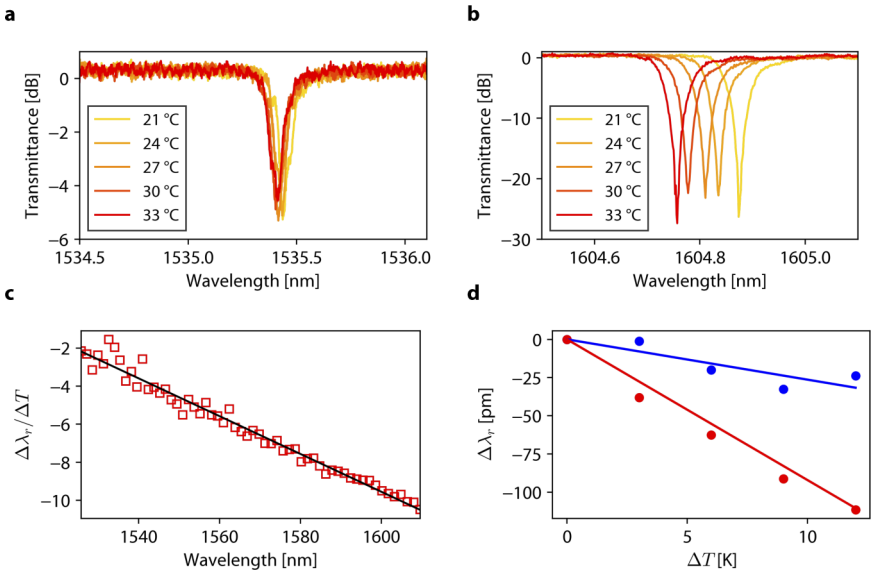

Fig. 7. Thermal measurements of a $As_{20}S_{80}$ clad SWG with $\Lambda = 250$ nm, $DC = 0.5$ and $w = 450$ nm. (a,b) Normalized transmittance of a single resonance with a low (a) and high (b) thermo-optic coefficient. (c) Temeperature dependent resonance shift coefficient $\Delta\lambda_r/\Delta T$ measured over the C+L band. Linear fits used to extract $\Delta\lambda_r/\Delta T$ from the resonances shown in blue (a) and red (b).

The resonance shift $\Delta\lambda_r$ is extracted for each measured trace and a linear fit is used to extract the resonance shift coefficient $\Delta\lambda_r/\Delta T$. Two examples of this process are shown in Fig. 7(d) while the full wavelength dependent data is shown in Fig. 7(c). $\Delta\lambda_r/\Delta T$ decreases at longer wavelength as the confinement factor with the negative *TOC* $As_{20}S_{80}$ increases. Thermal compensation between the silicon positive *TOC* and ChG negative *TOC* is nearly perfect at shorter wavelengths. The minimum value measured is $\Delta\lambda_r/\Delta T = -1.54$ pm/K, indicating that the hybrid MR is virtually athermal at this wavelength. The value of $\Delta\lambda_r/\Delta T$ is slightly lower than the one predicted in Sect.2. using FDTD simulation. This discrepancy could arise from difference between the simulated and fabricated SWG, similar to the effect on group index noted in sect.4.1. We also note that the deposited cladding was slightly thicker than in the simulation (by 90 nm) thus slightly increasing the overlap with the chalcogenide. We note that the athermal wavelength could be shifted, resulting in a zero crossing of $\Delta\lambda_r/\Delta T$, by slightly adjusting the geometry of the waveguide. Increasing the feature size of the silicon will reduce Γ_{clad} and shift the curve in Fig. 7(c) upwards. It is also interesting to calculate the effective thermo-optic coefficient of waveguide $TOC_{eff} = dn_{eff}/dT$, which can be obtained from measurements using the expression [40,41]

$$\frac{d\lambda_r}{dT} = \frac{\lambda_r}{n_g}\left(n_{eff}\alpha_{sub} + \frac{dn_{eff}}{dT}\right), \tag{5}$$

where we assumed that the thermal expansion is governed by the silicon substrate expansion coefficient $\alpha_{sub} = 2.6 \times 10^{-6}$. The effective index is taken from simulation while the other values are from measurements. Using Eq. (5), the minimum effective *TOC* is -2.93×10^{-6} RIU/K. This value further confirms the extremely low thermal dependence achieved in the hybrid SWG. This

Optics EXPRESS

demonstration of nearly perfect athermality is exemplary of the flexibility of SWG in engineering light-matter interactions. As such, SWGs are excellent candidates for hybrid integration, where the properties of exotic materials are used to enhance silicon photonics. It is also important to emphasize that the use of the hybrid chalcogenide-silicon SWG proposed in this work goes beyond thermal compensation and could find application in various important fields including Brillouin photonics [19], amplifiers [42] or reconfigurable photonics [43].

5. Conclusion

In summary, we demonstrated a novel heterogeneous silicon subwavelength grating waveguide with a high-index chalcogenide glass cladding that exhibits athermal operation and propagation loss of 8.6 dB/cm. Further work will focus on using the athermal SWG in concrete applications and improve the loss performance. This work demonstrates the potential of heterogeneous SWGs to engineer light-matter interaction for some of the most critical challenges facing silicon photonics.

Funding. Natural Sciences and Engineering Research Council of Canada (STPGP 494358-16); Canada First Research Excellence Fund (Sentinel North).

Acknowledgments. The authors would like to thank Stéphan Gagnon and Wagner Correr for the SEM/FIB images.

Disclosures. The authors declare no conflicts of interest.

Data availability. Data underlying the results presented in this paper are not publicly available at this time but maybe obtained from the authors upon reasonable request.

References

1. P. Cheben, R. Halir, J. H. Schmid, H. A. Atwater, and D. R. Smith, "Subwavelength integrated photonics," Nature **560**(7720), 565–572 (2018).
2. P. J. Bock, P. Cheben, J. H. Schmid, J. Lapointe, A. Delâge, S. Janz, G. C. Aers, D.-X. Xu, A. Densmore, and T. J. Hall, "Subwavelength grating periodic structures in silicon-on-insulator: a new type of microphotonic waveguide," Opt. Express **18**(19), 20251–20262 (2010).
3. P. Cheben, P. J. Bock, J. H. Schmid, J. Lapointe, S. Janz, D.-X. Xu, A. Densmore, A. Delâge, B. Lamontagne, and T. J. Hall, "Refractive index engineering with subwavelength gratings for efficient microphotonic couplers and planar waveguide multiplexers," Opt. Lett. **35**(15), 2526–2528 (2010).
4. Y. Wang, H. Sun, M. Khalil, W. Dong, I. Gasulla, J. Capmany, and L. R. Chen, "On-chip optical true time delay lines based on subwavelength grating waveguides," Opt. Lett. **46**(6), 1405–1408 (2021).
5. P. Jean, A. Gervais, S. LaRochelle, and W. Shi, "Slow light in subwavelength grating waveguides," IEEE J. Sel. Top. Quantum Electron. **26**(2), 1–8 (2020).
6. D. Charron, J. St-Yves, O. Jafari, S. LaRochelle, and W. Shi, "Subwavelength-grating contradirectional couplers for large stopband filters," Opt. Lett. **43**(4), 895–898 (2018).
7. R. Halir, P. Cheben, J. M. Luque-González, J. D. Sarmiento-Merenguel, J. H. Schmid, G. Waguemert-Pérez, D.-X. Xu, S. Wang, A. Ortega-Monux, and I. Molina-Fernandez, "Ultra-broadband nanophotonic beamsplitter using an anisotropic sub-wavelength metamaterial," Laser Photonics Rev. **10**(6), 1039–1046 (2016).
8. J. M. Luque-Gonzalez, A. Herrero-Bermello, A. Ortega-Monux, I. Molina-Fernandez, A. V. Velasco, P. Cheben, J. H. Schmid, S. Wang, and R. Halir, "Tilted subwavelength gratings: controlling anisotropy in metamaterial nanophotonic waveguides," Opt. Lett. **43**(19), 4691–4694 (2018).
9. X. Guan, P. Chen, S. Chen, P. Xu, Y. Shi, and D. Dai, "Low-loss ultracompact transverse-magnetic-pass polarizer with a silicon subwavelength grating waveguide," Opt. Lett. **39**(15), 4514–4517 (2014).
10. P. Cheben, J. H. Schmid, S. Wang, D.-X. Xu, M. Vachon, S. Janz, J. Lapointe, Y. Painchaud, and M.-J. Picard, "Broadband polarization independent nanophotonic coupler for silicon waveguides with ultra-high efficiency," Opt. Express **23**(17), 22553–22563 (2015).
11. T. Barwicz, Y. Taira, T. W. Lichoulas, N. Boyer, Y. Martin, H. Numata, J. Nah, S. Takenobu, A. Janta-Polczynski, E. L. Kimbrell, R. Leidy, M. H. Khater, S. Kamlapurkar, S. Engelmann, Y. A. Vlasov, and P. Fortier, "A novel approach to photonic packaging leveraging existing high-throughput microelectronic facilities," IEEE J. Sel. Top. Quantum Electron. **22**(6), 455–466 (2016).
12. P. Cheben, J. Čtyroký, J. H. Schmid, S. Wang, J. Lapointe, J. G. Wanguemert-Perez, I. Molina-Fernandez, A. Ortega-Monux, R. Halir, D. Melati, D. Xu, S. Janz, and M. Dado, "Bragg filter bandwidth engineering in subwavelength grating metamaterial waveguides," Opt. Lett. **44**(4), 1043–1046 (2019).
13. H. Yan, L. Huang, X. Xu, S. Chakravarty, N. Tang, H. Tian, and R. T. Chen, "Unique surface sensing property and enhanced sensitivity in microring resonator biosensors based on subwavelength grating waveguides," Opt. Express **24**(26), 29724–29733 (2016).

Optics EXPRESS

14. J. G. Wanguemert-Perez, P. Cheben, A. Ortega-Monux, C. Alonso-Ramos, D. Perez-Galacho, R. Halir, I. Molina-Fernandez, D.-X. Xu, and J. H. Schmid, "Evanescent field waveguide sensing with subwavelength grating structures in silicon-on-insulator," Opt. Lett. **39**(15), 4442–4445 (2014).
15. J. H. Schmid, M. Ibrahim, P. Cheben, J. Lapointe, S. Janz, P. J. Bock, A. Densmore, B. Lamontagne, R. Ma, W. N. Ye, and D.-X. Xu, "Temperature-independent silicon subwavelength grating waveguides," Opt. Lett. **36**(11), 2110–2112 (2011).
16. C. M. Naraine, J. W. Miller, H. C. Frankis, D. E. Hagan, P. Mascher, J. H. Schmid, P. Cheben, A. P. Knights, and J. D. B. Bradley, "Subwavelength grating metamaterial waveguides functionalized with tellurium oxide cladding," Opt. Express **28**(12), 18538–18547 (2020).
17. B. J. Eggleton, B. Luther-Davies, and K. Richardson, "Chalcogenide photonics," Nat. Photonics **5**(3), 141–148 (2011).
18. R. Pant, C. G. Poulton, D.-Y. Choi, H. Mcfarlane, S. Hile, E. Li, L. Thevenaz, B. Luther-Davies, S. J. Madden, and B. J. Eggleton, "On-chip stimulated brillouin scattering," Opt. Express **19**(9), 8285–8290 (2011).
19. Y. Liu, A. Choudhary, G. Ren, K. Vu, B. Morrison, A. Casas-Bedoya, T. G. Nguyen, D.-Y. Choi, P. Ma, A. Mitchell, S. J. Madden, D. Marpaung, and B. J. Eggleton, "Integration of brillouin and passive circuits for enhanced radio-frequency photonic filtering," APL Photonics **4**(10), 106103 (2019).
20. S. Serna, H. Lin, C. Alonso-Ramos, C. Lafforgue, X. L. Roux, K. A. Richardson, E. Cassan, N. Dubreuil, J. Hu, and L. Vivien, "Engineering third-order optical nonlinearities in hybrid chalcogenide-on-silicon platform," Opt. Lett. **44**(20), 5009–5012 (2019).
21. A. Yariv and P. Yeh, *Photonics: Optical Electronics in Modern Communications (The Oxford Series in Electrical and Computer Engineering)* (Oxford University Press, Inc., USA, 2006).
22. J. Grgić, J. R. Ott, F. Wang, O. Sigmund, A.-P. Jauho, J. Mørk, and N. A. Mortensen, "Fundamental limitations to gain enhancement in periodic media and waveguides," Phys. Rev. Lett. **108**(18), 183903 (2012).
23. J. P. Hugonin, P. Lalanne, T. P. White, and T. F. Krauss, "Coupling into slow-mode photonic crystal waveguides," Opt. Lett. **32**(18), 2638–2640 (2007).
24. P. Velha, J. P. Hugonin, and P. Lalanne, "Compact and efficient injection of light into band-edge slow-modes," Opt. Express **15**(10), 6102–6112 (2007).
25. N. Mann, M. Patterson, and S. Hughes, "Role of bloch mode reshaping and disorder correlation length on scattering losses in slow-light photonic crystal waveguides," Phys. Rev. B **91**(24), 245151 (2015).
26. N. A. Mortensen and S. Xiao, "Slow-light enhancement of beer-lambert-bouguer absorption," Appl. Phys. Lett. **90**(14), 141108 (2007).
27. A. Gervais, P. Jean, W. Shi, and S. LaRochelle, "Design of slow-light subwavelength grating waveguides for enhanced on-chip methane sensing by absorption spectroscopy," IEEE J. Sel. Top. Quantum Electron. **25**(3), 1–8 (2019).
28. J. P. Dowling, M. Scalora, M. J. Bloemer, and C. M. Bowden, "The photonic band edge laser: A new approach to gain enhancement," J. Appl. Phys. **75**(4), 1896–1899 (1994).
29. V. B. Novikov and T. V. Murzina, "Borrmann effect in photonic crystals," Opt. Lett. **42**(7), 1389–1392 (2017).
30. W. N. Ye, J. Michel, and L. C. Kimerling, "Athermal high-index-contrast waveguide design," IEEE Photonics Technol. Lett. **20**(11), 885–887 (2008).
31. P. Jean, A. Douaud, T. Thibault, S. LaRochelle, Y. Messaddeq, and W. Shi, "Sulfur-rich chalcogenide claddings for athermal and high-q silicon microring resonators," Opt. Mater. Express **11**(3), 913–925 (2021).
32. S. Feng, K. Shang, J. T. Bovington, R. Wu, B. Guan, K.-T. Cheng, J. E. Bowers, and S. J. B. Yoo, "Athermal silicon ring resonators clad with titanium dioxide for 1.3μm wavelength operation," Opt. Express **23**(20), 25653–25660 (2015).
33. B. J. Frey, D. B. Leviton, and T. J. Madison, "Temperature-dependent refractive index of silicon and germanium," in *Optomechanical Technologies for Astronomy*, vol. 6273 E. Atad-Ettedgui, J. Antebi, and D. Lemke, eds., International Society for Optics and Photonics (SPIE, 2006), pp. 790–799.
34. L. Chrostowski, H. Shoman, M. Hammood, H. Yun, J. Jhoja, E. Luan, S. Lin, A. Mistry, D. Witt, N. A. F. Jaeger, S. Shekhar, H. Jayatilleka, P. Jean, S. B.. Villers, J. Cauchon, W. Shi, C. Horvath, J. N. Westwood-Bachman, K. Setzer, M. Aktary, N. S. Patrick, R. J. Bojko, A. Khavasi, X. Wang, T. Ferreira de Lima, A. N. Tait, P. R. Prucnal, D. E. Hagan, D. Stevanovic, and A. P. Knights, "Silicon photonic circuit design using rapid prototyping foundry process design kits," IEEE J. Sel. Top. Quantum Electron. **25**(5), 1–26 (2019).
35. H. Shiran, H. Rahbardar Mojaver, J. Bachman, C. Jin, and O. Liboiron-Ladouceur, "Impact of sio2 cladding voids in siph building blocks," in *2020 IEEE Photonics Conference (IPC)*, (2020), pp. 1–2.
36. P. Jean, A. Douaud, V. Michaud-Belleau, S. H. Messaddeq, J. Genest, S. LaRochelle, Y. Messaddeq, and W. Shi, "Etchless chalcogenide microresonators monolithically coupled to silicon photonic waveguides," Opt. Lett. **45**(10), 2830–2833 (2020).
37. P. Rabiei, W. H. Steier, C. Zhang, and L. R. Dalton, "Polymer micro-ring filters and modulators," J. Lightwave Technol. **20**(11), 1968–1975 (2002).
38. L. W. Luo, G. S. Wiederhecker, J. Cardenas, and M. Lipson, "High quality factor etchless silicon photonic ring resonators," Opt. Express **19**, 1328–1330 (2010).
39. J. D. Sarmiento-Merenguel, A. Ortega-Monux, J.-M. Fedeli, J. G. Wanguemert-Perez, C. Alonso-Ramos, E. Duran-Valdeiglesias, P. Cheben, I. Molina-Fernandez, and R. Halir, "Controlling leakage losses in subwavelength grating silicon metamaterial waveguides," Opt. Lett. **41**(15), 3443–3446 (2016).

Optics EXPRESS

40. J. Teng, P. Dumon, W. Bogaerts, H. Zhang, X. Jian, X. Han, M. Zhao, G. Morthier, and R. Baets, "Athermal silicon-on-insulator ring resonators by overlaying a polymer cladding on narrowed waveguides," Opt. Express **17**(17), 14627–14633 (2009).
41. Y. Kokubun, N. Funato, and M. Takizawa, "Athermal waveguides for temperature-independent lightwave devices," IEEE Photonics Technol. Lett. **5**(11), 1297–1300 (1993).
42. K. Yan, K. Vu, and S. Madden, "Internal gain in er-doped as2s3 chalcogenide planar waveguides," Opt. Lett. **40**(5), 796–799 (2015).
43. A. Canciamilla, F. Morichetti, S. Grillanda, P. Velha, M. Sorel, V. Singh, A. Agarwal, L. C. Kimerling, and A. Melloni, "Photo-induced trimming of chalcogenide-assisted silicon waveguides," Opt. Express **20**(14), 15807–15817 (2012).